# Nonprecious Bimetallic Iron–Molybdenum Sulfide Electrocatalysts for the Hydrogen Evolution Reaction in Proton Exchange Membrane Electrolyzers

Adina Morozan, Hannah Johnson, Camille Roiron, Ghislain Genay, Dmitry Aldakov, Ahmed Ghedjatti, Chuc T. Nguyen, Phong D. Tran, Sachin Kinge, Vincent Artero

# Nonprecious Bimetallic Iron-Molybdenum Sulfide Electrocatalysts for the Hydrogen Evolution Reaction in Proton-Exchange Membrane Electrolyzers

*Adina Morozan[✧,#], Hannah Johnson[§,#], Camille Roiron[✧], Ghislain Genay[✧], Dmitry Aldakov[⊡], Ahmed Ghedjatti[✧], Chuc T. Nguyen[△], Phong D. Tran[△], Sachin Kinge[§], Vincent Artero[✧,*]*

[✧]Univ. Grenoble Alpes, CNRS, CEA/IRIG, Laboratoire de Chimie et Biologie des Métaux, 17 rue des Martyrs, 38054 Grenoble, France

[§]Toyota Motor Europe, Advanced Technology, Hoge Wei 33, Zaventem 1930, Belgium

[⊡]Univ. Grenoble Alpes, CNRS, CEA/IRIG, SyMMES, STEP, 17 rue des Martyrs, 38054 Grenoble, France

[△]University of Science and Technology of Hanoi, Vietnam Academy of Science and Technology, 18 Hoang Quoc Viet, Ha Noi, Vietnam

KEYWORDS: iron-molybdenum sulfide, microwave irradiation, carbon nanotubes, hydrogen evolution reaction, proton exchange membrane electrolyzer, accelerated stress test

ABSTRACT

In this study, we report the synthesis and characterization of non-precious bimetallic iron-molybdenum sulfide bioinspired electrocatalysts for the hydrogen evolution reaction (HER). Iron-molybdenum sulfide materials were obtained through three distinct scalable synthetic approaches using microwave irradiation or heat treatment in furnace under inert and reductive atmospheres. These electrocatalysts were combined with carbon nanotubes (CNTs) and their activity for the hydrogen evolution reaction (HER) was studied in acidic environment. The most efficient composite material of the series was obtained by microwave synthesis and displays a current density per geometric area of 10 $mA \cdot cm^{-2}$ at an overpotential of 140 mV with unity faradaic efficiency for hydrogen evolution. This composite cathode catalyst was implemented into a proton exchange membrane (PEM) electrolyzer single cell with iridium black as anode catalyst and could be operated at 0.5 $A \cdot cm^{-2}$ requiring less than 300 mV additional voltage compared to Pt, and with remarkable stability during accelerated stress testing.

## INTRODUCTION

Renewable energy generation capacity has been increasing significantly in recent years as a way towards a clean and sustainable energy system for reducing air pollution and limiting the increase in average global temperature.[1] Power to hydrogen is deemed to be a promising solution for storing intermittent renewable energy such as wind or solar. “Green hydrogen” is an efficient energy carrier that can be exploited directly via its use in fuel cell systems, indirectly as an alternative to fossil fuel technology for transportation, residential and industrial heating, or as a feedstock for the synthesis of commodity chemicals and fertilisers.[2-3] The market size of hydrogen and fuel cells is expected to grow to 2.5 trillion US dollars by 2050.[4]

Although hydrogen is already cheaply produced at industrial scales through conventional methods, such as steam methane reforming or coal gasification,[5-6] only 4 % of global $H_2$ needs are covered by $CO_2$ emission-free water electrolysis,[7] which is currently the most promising option for a sustainable hydrogen production.[8] Alkaline electrolysis is a mature technology in the large-scale industrial sector with currently lower cost.[9-11] This technology has nevertheless major drawbacks such as the use of liquid electrolyte, high ohmic losses, $H_2$ crossover or low operating pressure, associated with high maintenance costs and low adaptability to fluctuating power supply – a characteristic of renewable energy.[12-14] An alternative technology is proton exchange membrane (PEM) electrolysis, which has advantages such as compact design, quick response, higher efficiency (80-90 %), higher current density (ca. $2A \cdot cm^{-2}$) and tolerance of large variations (0.1 W to 100 kW) in power input.[7, 13, 15] PEM electrolysis is a technology with significant cost reduction potential and is expected to have a commercial advantage over alkaline electrolysis by 2030.[16]

Typically, in PEM electrolysis (acidic environment), highly active and stable precious metal based electrocatalysts are used, such as Pt-based catalysts at the cathode for the hydrogen evolution reaction (HER)[17-18] and Ir or Ru-based catalysts at the anode for the oxygen evolution reaction (OER).[19-20] Although catalyst cost is not currently the main cost driver for PEM electrolysis, it will become important in the long-term as demand increases for rare and expensive precious metals.[14, 21-22]

The challenges towards HER in PEM electrolysis have focused on the development of efficient, cost-effective and stable noble metal-free electrocatalysts for the cathode. Natural hydrogenases and nitrogenases enzymes are effective catalysts for HER,[23-24] and their active sites consist of (bi)metal sulfide clusters based on Earth-abundant metals such as Fe, Ni, and Mo.

While the HER activity of crystalline molybdenum sulfide (c-$MoS_2$) was reported in the 1970's,[25] it was only more recently highlighted by Hinnemann et al.[26] and Jaramillo et al.[27] that its edge sites are inorganic analogues of the nitrogenase active site for electrochemical hydrogen evolution. This triggered a large number of studies of such bio-inspired catalysts based on single metal sulfides.[28-29] Later on, it was demonstrated that the electrocatalytic activity of metal sulfides was improved by the combination with other metal ions, such cobalt sulfide,[30] cobalt doped-$FeS_4$,[31] Ni-Mo-S nanostructures,[32] Co-Mo-S and Co-W-S structures,[33-34] V- or Zn-doped $MoS_2$.[35-36] In particular the promotional effect of iron on the HER activity of molybdenum sulfides, as in Fe-$MoS_3$,[37] $FeS_2$-doped $MoS_2$[38] and amorphous $FeMoS_4$[39] have been reported. The structure-composition-activity relationships for these systems are thus highly regulated by the incorporation of a second metal. Subsequently, tuning of electronic mobility, charge transportability, density of electrocatalytically active sites and turnover frequency has led to improved HER activity by lowering the overpotential requirement. However, the reported synthetic methods for bimetallic sulfide materials are rarely scalable and only few studies report the practical implementation of metal sulfide catalysts into PEM electrolyzers[40] and they have been restricted to single metal sulfide materials such as $MoS_2$,[41] amorphous $MoS_x$,[42-44] $[Mo_3S_{13}]^{2-}$ nanoclusters[42] and $FeS_2$.[45]

We report here the development of bimetallic iron-molybdenum sulfides as new bioinspired non-precious catalysts for HER. We describe scalable synthetic methods and characterization of these materials, their activity towards the HER in combination with carbon nanotubes (CNTs) and their integration as cathode catalyst into a proton exchange membrane (PEM) electrolyzer.

## EXPERIMENTAL SECTION

*Materials and reagents*

Catalysts were prepared by using molybdenum chloride ($MoCl_3$ and $MoCl_5$), iron chloride ($FeCl_3$) and thiourea as precursors, as well as ethylene glycol (EG), all purchased from Sigma Aldrich. All chemical reagents used in this study were of analytical grade and were used as received without further purification. Commercial grade NC7000 multi-walled carbon nanotubes (denoted CNTs) were obtained from Nanocyl (Belgium) and Nafion 117 solution (5 wt % in a mixture of lower aliphatic alcohols and water) was obtained from Sigma-Aldrich. Sigracet 39-BC gas diffusion layer (GDL) was purchased from SGL Carbon GmbH, Germany and Vulcan XC72R from Cabot (Switzerland). Nafion NRE-212 membrane (50 μm thick, Alfa-Aesar) and iridium black powder (Sigma-Aldrich) were used for the fabrication of the membrane electrode assembly (MEA). The electrolyte used, $H_2SO_4$ (0.5 M) aqueous solution, was prepared with ultrapure water (18.2 MΩ·cm resistivity at 25 °C).

*Synthesis*

In the microwave synthesis, appropriate amounts of metal salts ($MoCl_3$: 0.5 mmol, 135.2 mg and $FeCl_3 \cdot H_2O$: 0.5 mmol, 101.1 mg) and thiourea (1.5 mmol, 114.2 mg) precursors were mixed in EG (10 ml). After stirring for 5 min, the solution was then placed in a Discover SP microwave synthesizer in a special 30 ml vial and the reaction was conducted under the following conditions: irradiation varying from 0 to 300 W in order to maintain the temperature at 255 °C leading to the pressure of 8 bars for 20 min. The resulting high-viscosity black precipitate was transferred into ethanol for centrifugation. Then the precipitate was washed under centrifugation for several times with ethanol and distilled water until the supernatant was clear. The final precipitate (ca 130 mg) was vacuum dried overnight and then collected for characterization. The obtained sample was denoted as $FeMoS_{(mw)}$.

By the heat treatment method, appropriate amounts of metal salts ($MoCl_5$: 1.8 mmol, 492 mg and $FeCl_3 \cdot H_2O$: 1.8 mmol, 487 mg) and thiourea (5.4 mmol, 412 mg) precursors were dispersed in ethanol under magnetic stirring. The resulting dry powder after solvent evaporation was transferred into a alumina boat, inserted into a quartz tube and heated at 5 °C·min$^{-1}$ up to 550 °C in a flowing atmosphere (Ar or Ar+$H_2$), held at this temperature for 2 h, then allowed to cool down to RT. The resulting samples were denoted as $FeMoS_{(HT,\ Ar)}$ (ca. 120 mg) and $FeMoS_{(HT,\ Ar+H2)}$ ca. 120 mg).

Scale-up can be achieved either by repetitive synthesis, which has the advantage of being facile, fast and automated for the microwave approach, or by starting from higher amount of precursors for the heat treatment approach. The reference materials without iron were also prepared, whose synthesis follows otherwise the synthetic steps described above. The obtained reference samples were denoted as $MoS_{(mw)}$ (ca. 120 mg obtained from 0.5 mmol-135.2 mg $MoCl_3$ and 1.5 mmol-114.2 mg thiourea in 10 ml of EG), $MoS_{(HT,\ Ar)}$ and $MoS_{(HT,\ Ar+H2)}$ (ca. 130 mg of each, obtained from 1.8 mmol - 492 mg $MoCl_5$ and 5.4 mmol - 412 mg thiourea in 20 ml of ethanol).

*Physical and chemical characterization*

Raman analysis was conducted on a NRS-7100 Laser Raman spectrometer (JASCO, Japan) using a 532 nm green line laser. Prior to measurement, wavelength calibration was done using the bulk Si peak at 520 cm$^{-1}$ as a standard reference.

X-ray diffraction (XRD) analysis was carried out using a Rigaku Miniflex 600 diffractometer with a CuKα radiation (λ = 0.15406 nm).

Scanning electron microscopy (SEM) images were recorded with a scanning electron microscope Zeiss Ultra 55 (acceleration tension 5 kV).

Transmission electron microscopy (TEM) images and selected-area electron diffraction (SAED) patterns were acquired with a Cs-probe corrected FEI Titan Themis transmission electron microscope, operated at 80 kV. A catalyst suspension in ethanol was prepared by ultrasonic homogenization and was then drop-cast on an ultrathin carbon film on a Cu grid. High-angle annular dark-field scanning transmission electron microscopy (HAADF-STEM) and corresponding energy-dispersive spectroscopy (EDS) elemental mapping analyses were collected with on an FEI–Osiris microscope operated at 200 kV.

X-ray photoelectron spectroscopy (XPS) analyses were carried out with a Versa Probe II spectrometer (ULVAC-PHI) equipped with a monochromated Al Kα source (hν = 1486.6 eV). The core level peaks were recorded with constant pass energy of 23.3 eV. The XPS spectra were fitted with CasaXPS 2.3 software using Shirley background. Binding energies are referenced with respect to the adventitious carbon (C 1s BE = 284.6 eV).

Inductively coupled plasma atomic emission spectrometry (ICP-AES) measurements were carried out on a Shimadzu 9000 apparatus. The powder samples were completely dissolved by sonicating in 70 % nitric acid and then diluted to obtain a solution of ca. 1000 $\mu g \cdot L^{-1}$ of catalyst in 10 % nitric acid.

*Electrode preparation*

Electrochemical activity of the materials towards the HER was determined using a gas diffusion electrode (GDE) as working electrode. A catalyst ink including 1 mg of electrocatalyst, 160 µL of ethanol, 40 µL of water, 10 µL of 5 wt. % Nafion solution and optionally 0.2 mg of CNTs, was prepared by sonication. Then, aliquots of 10 µl of the ink were successively deposited on the microporous layer of a GDL piece (∅ 5 mm, 0.196 $cm^2$) to reach various catalyst loadings (0.24, 0.48, 0.97 and 1.46 $mg \cdot cm^{-2}$). The working GDE with the deposited

electrocatalyst layer was used in a conventional three-electrode electrochemical cell configuration.

Another electrode was prepared in a similar manner, but the electrocatalyst layer was deposited onto a glassy carbon disk (∅ 7 mm, 0.38 $cm^2$, catalyst loading of 0.97 $mg \cdot cm^{-2}$) instead of a GDL. This electrode was used for the electrochemical measurements coupled to gas chromatography to determine the faradaic yield of the electrode for $H_2$-evolution.

*Electrochemical measurements*

A detailed investigation of the electrocatalytic activity towards the HER was evaluated in $N_2$-saturated electrolyte (0.5 M $H_2SO_4$) using in a half-cell holder for GDE setup. The electrochemical experiments were performed in a continuously degassed electrolyte by nitrogen bubbling, in a three-electrode cell configuration and using a SP300 Bio-Logic potentiostat. The counter electrode consisted of a Ti wire and the reference electrode was an Ag/AgCl, KCl (3 M) (denoted below Ag/AgCl). The working electrode was a GDL substrate with the deposited electrocatalyst layer fixed in the half-cell holder[46] (Figure S1). A nitrogen gas flow at the surface of the GDL was used to remove the produced $H_2$. The pipe used to evacuate the gas was also used as the contact with the modified GDL.

All curves were iR-corrected by carrying out automatically ohmic drop compensation by the EC-Lab software using the electrochemical impedance technique (ZIR). Current densities were normalized in reference to the geometric area of the exposed electrode (0.056 $cm^2$). All potentials were reported vs. the Reversible Hydrogen Electrode (RHE) potential using the following equation: $E_{vs\ RHE} = E_{vs\ Ag/AgCl} - E_{Ag/AgCl\ vs\ NHE} + 0.059 \times pH$. The Ag/AgCl reference electrode was calibrated with the $[Fe(CN)_6]^{3-}/[Fe(CN)_6]^{4-}$ couple in an external electrochemical setup. Calibration against the $[Fe(CN)_6]^{3-}/[Fe(CN)_6]^{4-}$ couple was performed with a glassy

carbon electrode and a platinum wire as working and auxiliary electrodes, respectively, in 0.1 M potassium phosphate buffer (pH 7). The potential of the $[Fe(CN)_6]^{3-}/[Fe(CN)_6]^{4-}$ couple is denoted below as $E_{Fe(III)/Fe(II)\ vs\ Ag/AgCl}$ (0.225 V) and $E_{Fe(III)/Fe(II)\ vs\ NHE}$ (0.425 V) refers to the tabulated value of $E_{Fe(III)/Fe(II)}$ against the NHE potential.[47] Thus, $E_{Ag/AgCl\ vs\ NHE}$ is 0.200 V. Polarization curves were recorded using the linear sweep voltammetry (LSV) technique at a scan rate of 10 $mV \cdot s^{-1}$ and 25 °C, under a back-flow of $N_2$.

The stability tests were conducted by chronopotentiometry measurements (CP) under $N_2$-saturated electrolyte. The constant applied current corresponds to attained current density of −10 $mA \cdot cm^{-2}$.

*Electrochemical measurements coupled to gas chromatography*

The measurements were carried out in a three-electrode electrochemical cell in aqueous $H_2SO_4$ solution (0.5 M) and using a glassy carbon disk substrate (∅ 7 mm, 0.38 $cm^2$) for the preparation of the working electrode. Chronoamperometry (CA) measurements were performed for 4 h at a fixed potential of −160 mV vs RHE. The working and reference electrodes were placed in the same compartment filled with the electrolyte. The counter electrode was separated from the main compartment by keeping it in a bridge tube with ceramic junction filled with the electrolyte in order to avoid the poisoning with the released oxygen. In the in-line gas chromatography configuration,[48] the compartment of the working electrode is continuously flushed by $N_2$ carrier gas, whose rate was fixed through a Bronkhorst EL Flow Select mass flowmeter at 5 $ml \cdot min^{-1}$. The output gas was analyzed with a PerkinElmer Clarus 500 gas chromatograph with a porapak Q 80/100 column (6′x1/8″). The gas chromatograph was mounted in the so-called continuous flow mode in which the carrier gas stream fills an injection loop of 100 μL in the gas

chromatograph. The content of the injection loop is fed every 2 min into the gas chromatograph setup, where gases ($H_2$ and $O_2$) are separated and the area under the $H_2$ peak is computed.

Control calibrations were performed via chronopotentiometric experiments at cathodic current of −1 mA, in which a platinum mesh was used as the working electrode to evolve hydrogen from an aqueous $H_2SO_4$ solution (0.1 M). In these control experiments, the faradaic yields are assumed to be unitary, which allows the determination of calibration constant including all experimental biases of continuous flow setup. This value was then used to relate the area under the $H_2$ peak given by the in-line gas chromatograph setup to the experimentally measured production rate of $H_2$ in the electrochemical cell ($\eta_{meas}$). The theoretical production rate ($\eta_{theo}$) for $H_2$ derived from the charge Q passed in the cell, assuming a unitary faradaic yield, is calculated following the formula: $\eta_{theo} = Q/(2 \times F)$ where F is the Faraday constant (F = 96485 $C \cdot mol^{-1}$). The $\eta_{meas}/\eta_{theo}$ ratio then gives the faradaic yield of the electrode for $H_2$-evolution.

*Fabrication of membrane-electrodes assembly (MEA) for PEM electrolysis*

The membrane-electrode assembly (MEA) was prepared using Nafion NRE-212 membrane (50 μm thick) as the polymer electrolyte membrane, iridium black as the anode catalyst with a fixed loading of 2 $mg \cdot cm^{-2}$ and $FeMoS_{(mw)}$ as the cathode catalyst. For the cathode preparation, the $FeMoS_{(mw)}$ catalyst was mixed in a 1:1 mass ratio with carbon Vulcan XC72R, and the total loading (catalyst+carbon) was fixed at 4 $mg \cdot cm^{-2}$. Cathode catalyst ink was prepared using a 1.2/1 ethanol/water solution and Nafion ionomer (5 wt. % solution) corresponding to a Nafion-to-(catalyst+carbon) ratio of 1.4. The catalyst ink solutions were sonicated for ca. 1 h using an ultrasonic bath prior to deposition.

The anode catalyst ink was deposited by drop-casting onto a 5 $cm^2$ area of a decal substrate (PTFE-coated fiberglass cloth, Plastic Elastomer) until the fixed catalyst loading was reached.

The cathode catalyst ink was deposited by drop-casting onto GDL piece (5 $cm^2$) to reach the fixed catalyst loading. The as-prepared electrode and the coated decal substrate were assembled by sandwiching the Nafion membrane and hot pressing at 120 °C for 90 s under 5 MPa. The anode catalyst was transferred onto one side of the Nafion membrane by peeling off the decal substrate following the hot-press process. A Pt-coated titanium mesh (127 μm thick, 5 $cm^2$ area, FuelCellStore) was added on the anode side without pressing during the PEM electrolyzer cell assembling.

Two reference MEAs were prepared: one with a 0.5 $mg \cdot cm^{-2}$ 60% Pt-Vulcan/carbon paper electrode (FuelCellStore) as cathode instead of the $FeMoS_{(mw)}$/GDL electrode, and the a second with only Vulcan XC72R at the cathode side.

The as-prepared MEAs were further assembled in a PEM electrolyzer single cell.

*PEM electrolyzer setup*

Electrolysis tests were performed using a 5 $cm^2$ PEM electrolyzer single cell (Scribner). The cell consisted of two aluminium end-plates, two current collector plates and two grooved plates (carbon at the cathode side and platinized titanium at the anode side). These plates, with machined serpentine flow field of 0.125" on the working area of 5 $cm^2$, facilitate the flow of water and produced gases ($H_2$ and $O_2$). The prepared MEA was sandwiched between the two grooved plates and clamped together with current collectors and end-plates using nuts and bolts. The cell was assembled with PTFE (polytetrafluoroethylene) gaskets (FuelCellStore) to give a compression of ca. 15 %.[49] The PEM electrolyzer setup (Figure S2) consists of the electrochemical reaction cell, a peristaltic pump system (PP1300, WVR) and water reservoir, and a computer-controlled potentiostat (VSP-300 Bio-Logic with a ±10 A/[0, 5] V booster). Electrolyzer testing was carried out at 80 °C (atmospheric pressure), with ultrapure water (Milli-

Q) continuously pumped to the anode side at 4 $mL \cdot min^{-1}$. Evolved gases ($O_2$ from anode and $H_2$ from cathode) were released to the atmosphere through the outlets of the cell.

The performance of MEA was evaluated by recording the polarization curves from 1 V to 2 V with a scan rate of 10 $mV \cdot s^{-1}$. The curves were iR-corrected by carrying out automatically ohmic drop compensation by the EC-Lab software using the electrochemical impedance technique (ZIR). Prior to recording the polarization curve, the MEA was kept at voltages ranging from 1.2 to 1.4 V with an interval of 0.1 V and then from 1.4 V to 2 V with an interval of 0.05 V, for 5 min at each potential.

In order to assess the durability of the MEA, an in situ accelerated stress test (AST) was carried out. This AST was continuously applied for 24 h and the method cycled between 0.05 $A \cdot cm^{-1}$ minimum intensity and a 0.5 $A \cdot cm^{-1}$ maximum intensity and was held at each intensity for 15 min each.

## RESULTS AND DISCUSSION

### *Synthesis and characterization*

The bimetallic iron-molybdenum sulfide materials were prepared from thiourea and Fe and Mo salts and in a molar ratio of 3:1:1 according to two simple and scalable approaches. The first approach involved a microwave synthesis in ethylene glycol (EG) as reaction and dispersion media, and the second one involved a heat treatment synthesis under controlled atmosphere. In both cases, metal salts and thiourea were dissolved (in EG and ethanol, respectively), resulting in the formation of metal-thiourea complexes.[50-51] These complexes undergo decomposition under the microwave irradiation (0-300 W, 255 °C, 8 bars) or annealing conditions (550 °C, Ar or $Ar/H_2$). The metal sulfide products resulting from microwave irradiation and heat treatments were named $FeMoS_{(mw)}$, $FeMoS_{(HT,\ Ar)}$ and $FeMoS_{(HT,\ Ar+H_2)}$, respectively. Table 1 lists the

different samples investigated in this study and summarizes their main characteristics. Samples without Fe precursor, named $MoS_{(mw)}$, $MoS_{(HT,\ Ar)}$ and $MoS_{(HT,\ Ar+H_2)}$, respectively, were also similarly prepared for comparison (SI).

The synthetic method directly impacts the morphology of the materials as can be seen in the SEM images in Figure 1 and Figure S3. $FeMoS_{(mw)}$ (Figure 1A) consists of spherical flower-like assembled particles with homogeneous size distribution around 100 nm. By contrast, $FeMoS_{(HT,\ Ar)}$ and $FeMoS_{(HT,\ Ar+H_2)}$ (Figure 1B and 1C) have a sponge-like structure with a rough, nanostructured surface arising from the agglomeration of the catalyst particles. These particles with irregular size and shape are bound together resulting in an interlocked structure leading to the formation of a porous network.

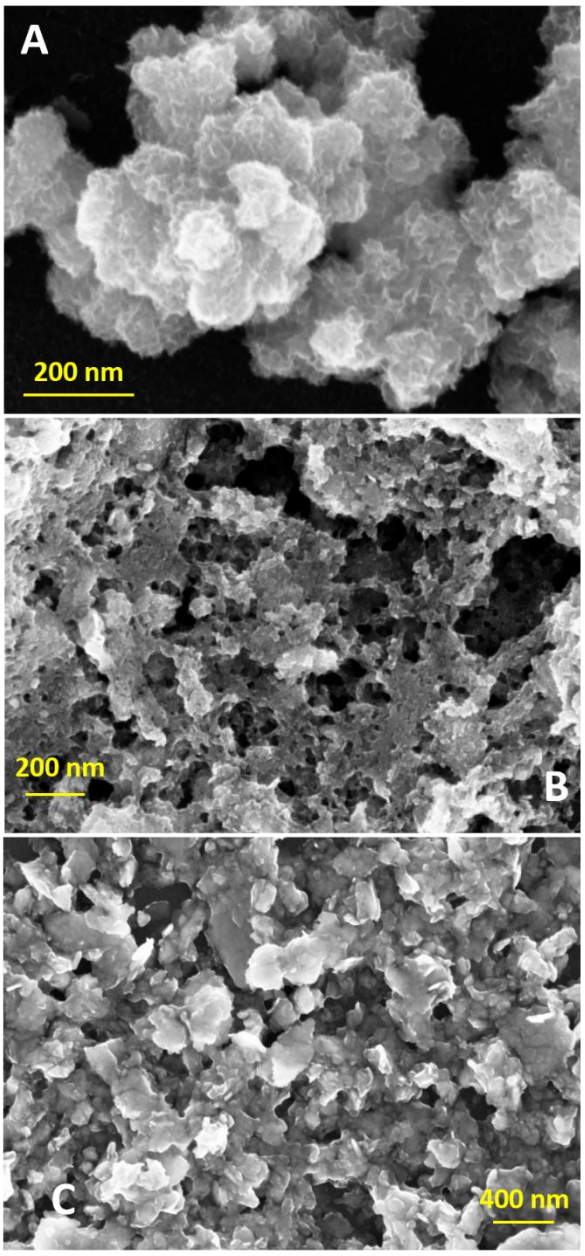


**Figure 1**. SEM images of (A) $FeMoS_{(mw)}$, (B) $FeMoS_{(HT,\ Ar)}$ and (C) $FeMoS_{(HT,\ Ar+H_2)}$.

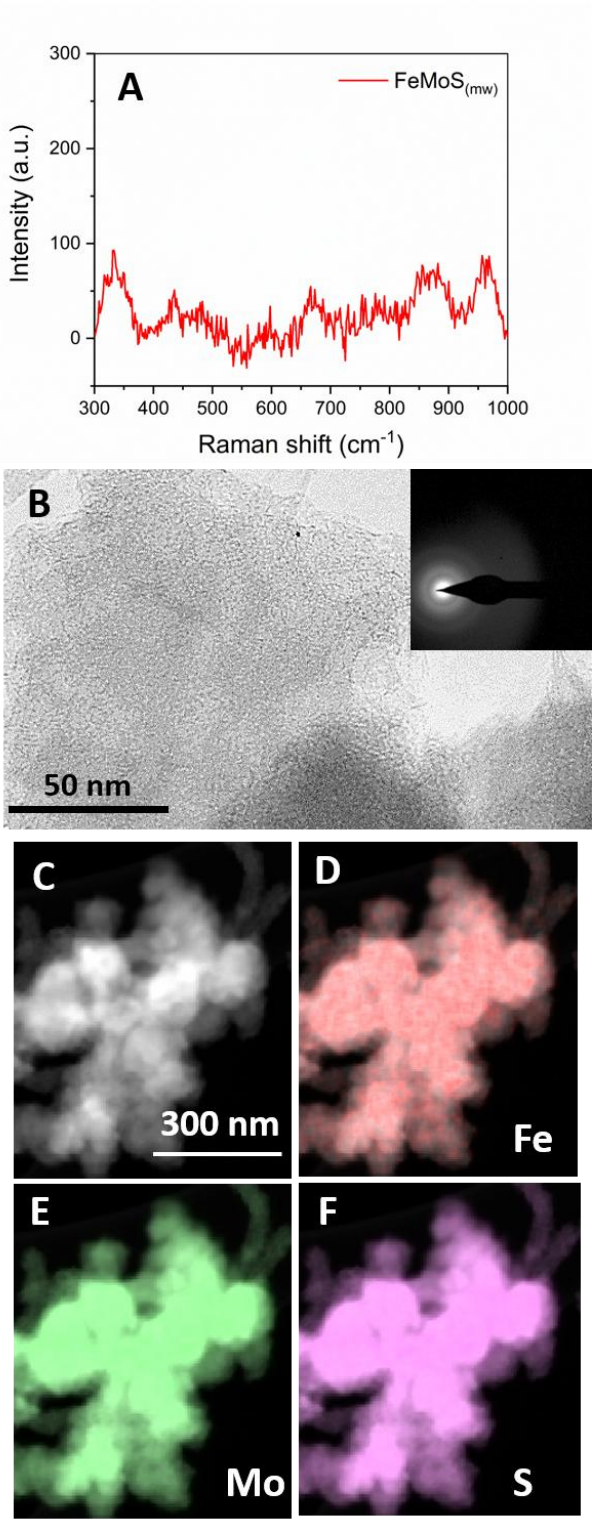


**Figure 2**. $FeMoS_{(mw)}$: (A). Raman spectra, (B) TEM and SAED images, (C) HAADF-STEM image and (D-F) corresponding EDS elemental mapping images of Fe, Mo and S.

The Raman spectrum of $FeMoS_{(mw)}$ (Figure 2A) showed a similar amorphous structure to $MoS_{(mw)}$ (Figure S4b) indicating no particular structural change by iron addition. The spectrum displays broad peaks between Raman shifts of 300 and 1000 $cm^{-1}$, indicating the amorphous nature of the sample. The molybdenum sulfide vibration modes of ν(Mo−S) at 300–400 $cm^{-1}$ and ν($Mo_3$−μS) at 455 $cm^{-1}$, which are characteristic for the amorphous nature (Figure S4a) are not well-defined and any defined vibration modes of bridging and terminal $S_2^{2-}$ could not be identified,[52-53] suggesting that there is no local structure. The Raman features at 800-1000 $cm^{-1}$ are assigned to molybdenum oxides defects[52] as well as to the possible presence of molybdenum oxysulfide $MoS_xO_y$.[54] The amorphous nature of $FeMoS_{(mw)}$ was further confirmed by XRD analysis (Figure S5a) as well as by TEM and SAED images (Figure 2B). The broad diffraction pattern with no discernable peaks clearly confirms the amorphous phase of the $FeMoS_{(mw)}$.[55-56] The characteristic halo ring pattern (Figure 2B, inset) is indeed characteristic for an amorphous material. The corresponding EDS mapping images show that Fe, Mo and S elements are homogeneously colocalized within the selected area of the material (Figure 2, D-F).

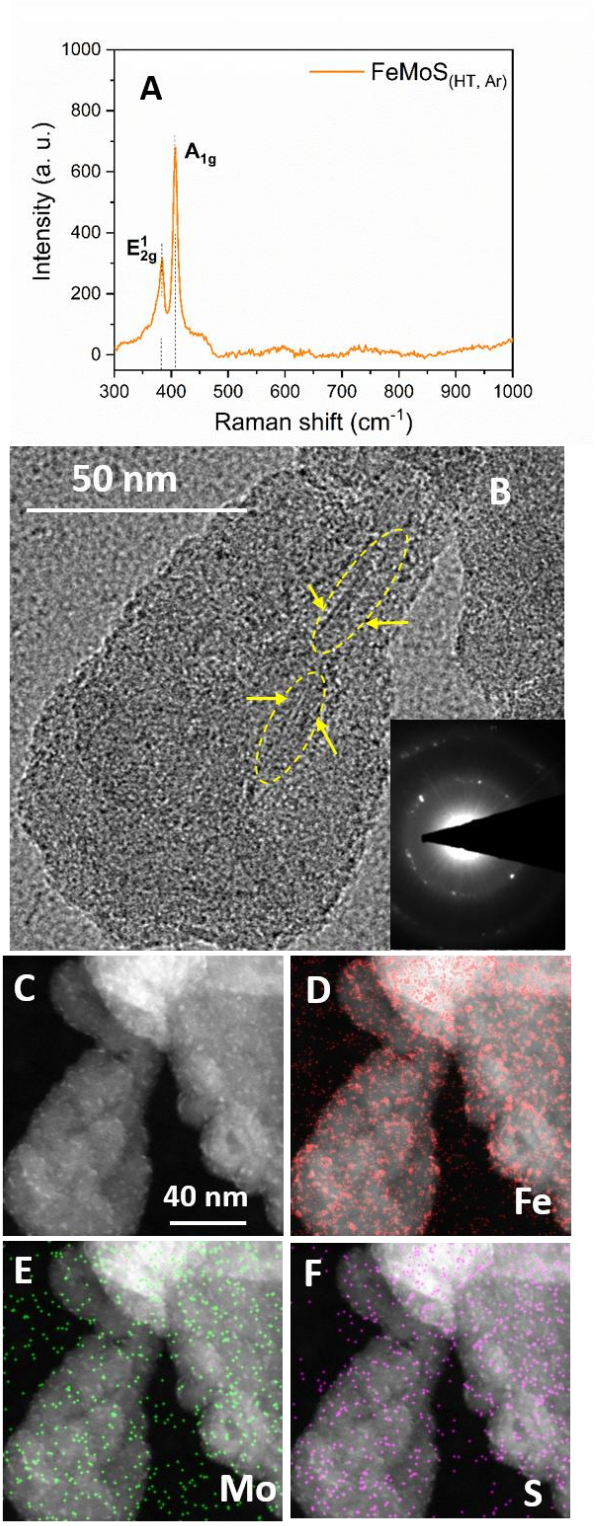


**Figure 3**. $FeMoS_{(HT,\ Ar)}$: (A). Raman spectra, (B) TEM and SAED images, (C) HAADF-STEM image and (D-F) corresponding EDS elemental mapping images of Fe, Mo and S.

The samples synthesized by heat treatment contain crystalline molybdenum sulfide, as revealed by well-defined Raman peaks (Figure 3A and 4A) at 384 $cm^{-1}$ and 407 $cm^{-1}$ corresponding to in-plane vibration ($E^1_{2g}$) and out-of-plane vibration ($A_{1g}$)[57-58] of $MoS_2$. The characteristic peak of $FeS_2$ at 342 $cm^{-1}$ as well as 378 $cm^{-1}$ could not be observed because of the low percentage of $FeS_2$ and/or overlapping by the peaks of $MoS_2$.[38, 59] The peak at 454 $cm^{-1}$ corresponds to the longitudinal acoustic phonon mode of $MoS_2$.[38] Iron seems to induce the crystallization process. The structure indeed evolves from amorphous for $MoS_{(HT,\ Ar)}$ (Figure S3c) to a crystalline one for $FeMoS_{(HT,\ Ar)}$ (Figure 3) in otherwise identical synthesis procedures. In XRD patterns (Figure S5a), the major peaks of $FeMoS_{(HT,\ Ar)}$ line up with those of $FeMoS_{(HT,\ Ar+H_2)}$. Both samples contain the characteristic diffraction peaks of the crystalline molybdenum sulfide (c-$MoS_2$) assigned to the planes indicated in Figure S5b.[60-63] The diffraction peaks at 30, 43, 53 and 63° indicate also the presence of crystalline Mo- and Fe, Mo-oxides phases.[64-65] When compared to $MoS_{(HT,\ Ar+H_2)}$ (Figure S5b), the addition of iron promotes the formation of the well-defined peaks at 36 and 43° (oxides and/or Fe, Mo-sulfide)[65-66] as well as at 48 and 65° (Figure S5a and b). The latter could both be associated with the presence of iron sulfide phases[67], although the peak at 48° can also indicate a higher crystallinity of the c-$MoS_2$ phase (105 plane) induced by the presence of iron and/or the reductive atmosphere during the synthesis. For the same iron loading, the degree of structural disorder seems related to the nature of the gas flow during the heat treatment, decreasing from $FeMoS_{(HT,\ Ar)}$ to $FeMoS_{(HT,\ Ar+H_2)}$. This behavior is observed from (i) the peaks intensity of the Raman spectra and the calculated full-width at half maximum intensity (FWHM) of peaks[68] (Figure 3A and 4A) and (ii) TEM analysis (Figure 3B and 4B). The corresponding EDS mapping images clearly show the presence of Fe, Mo and S elements in $FeMoS_{(HT,\ Ar)}$ Figure 3, D-F) and $FeMoS_{(HT,\ Ar+H_2)}$ (Figure 4, D-F). Compared to

$FeMoS_{(HT,\ Ar+H_2)}$, where Fe is mostly located in the center of the selected area, Fe is homogenously distributed in the entire bulk of in $FeMoS_{(HT,\ Ar)}$. By contrast, Mo and S elements are more uniformly distributed in the entire area of $FeMoS_{(HT,\ Ar+H_2)}$ compared to $FeMoS_{(HT,\ Ar)}$.

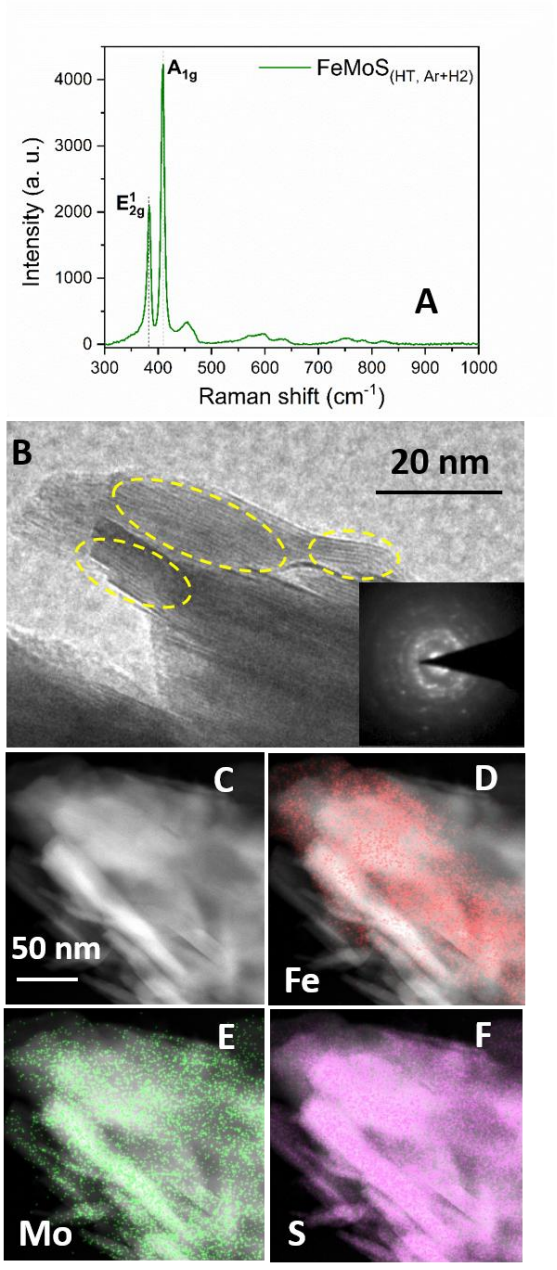


**Figure 4**. $FeMoS_{(HT,\ Ar+H_2)}$: (A). Raman spectra, (B) TEM and SAED images, (C) HAADF-STEM image and (D-F) corresponding EDS elemental mapping images of Fe, Mo and S.

**Table 1**. Main characteristics of the samples investigated in this study

| Sample | Synthetic approach | Structure | | Chemical composition | | $\eta_{10}^{HER}$ (mV) | Tafel slope ($mV \cdot dec^{-1}$) |
|---|---|---|---|---|---|---|---|
| | | Raman spectroscopy | Electronic microscopy | ICP-AES (bulk) | XPS (surface) | | |
| $FeMoS_{(mw)}$ | microwave | amorphous | amorphous | $Fe_{0.11}Mo_{1.14}S_2$ | $Fe_{0.04}Mo_{0.93}S_2$ | 140 | 57 |
| $FeMoS_{(HT, Ar)}$ | 550 °C, Ar | crystalline | crystalline | $Fe_{0.87}Mo_{0.76}S_2$ | $Fe_{0.42}Mo_{1.07}S_2$ | 206 | 126 |
| $FeMoS_{(HT, Ar+H2)}$ | 550 °C, Ar+$H_2$ | crystalline | crystalline | $Fe_{0.85}Mo_{0.91}S_2$ | $Fe_{0.42}Mo_{0.97}S_2$ | 180 | 101 |

ICP-AES measurements were performed to reveal the average bulk composition of the as-prepared materials (Table 1). The synthetic method influences directly the composition of the material. Despite the use of identical molar reactant ratios, the Fe content is eight times lower in $FeMoS_{(mw)}$ compared to both samples obtained by heat treatment. A slightly higher Mo content is found in $FeMoS_{(mw)}$ as compared to the other two (Fe, Mo)-sulfides.

The XPS data allowed resolving the chemical structure of the compounds studied. Although the samples display twice less Fe on the surface as compared to the bulk, the surface elemental distribution follows the bulk trends with much lower Fe content in the microwave-synthesized sample compared to the high temperature ones. Mo 3p and 3d spectra show the presence of the peaks clearly corresponding to molybdenum sulfide Mo-$S_x$ species (*ca*. 228.7 – 229.5 eV for $Mo3d_{5/2}$ and *ca*. 231.8 – 233 eV for $Mo3d_{3/2}$) (Figure 5A and S6). In all the cases, they coexist with Mo-$O_x$ compounds signature (232.4-232.8 eV and 236 eV),[39, 52, 69] the amount of which can be correlated with the mean oxidation state of molybdenum in the material. Indeed, for $FeMoS_{(HT, Ar)}$ produced from $MoCl_5$ the Mo-$O_x$/Mo-$S_x$ ratio reaches 77 % but the use of reducing $H_2$ atmosphere allows to maintain this ratio below 21 %. This ratio is slightly higher (36 %) for $FeMoS_{(mw)}$ produced from $MoCl_3$. The S2p spectra reveal a mixture of three sulfur doublets for

all three compounds: one corresponding to Mo and Fe sulfides (around 161.9 eV), another to polysulfides (163.0 eV), and finally one to $SO_4^{2-}$ (168.5 eV) (Figure 5B). The concentration of the sulfates is, as expected, the highest for the most oxidized $FeMoS_{(HT,\ Ar)}$ sample. Finally, the iron region can be fitted with several peaks indicating the main Fe oxidation state of +3 (711 and 715 eV), together with a weak $Fe^{III}$ satellite feature at 719 eV.[70] The presence of metallic Fe observed usually at 706.6 eV as well as $FeS_2$ (around 707 eV) was not observed in any of the three materials (Figure S7).

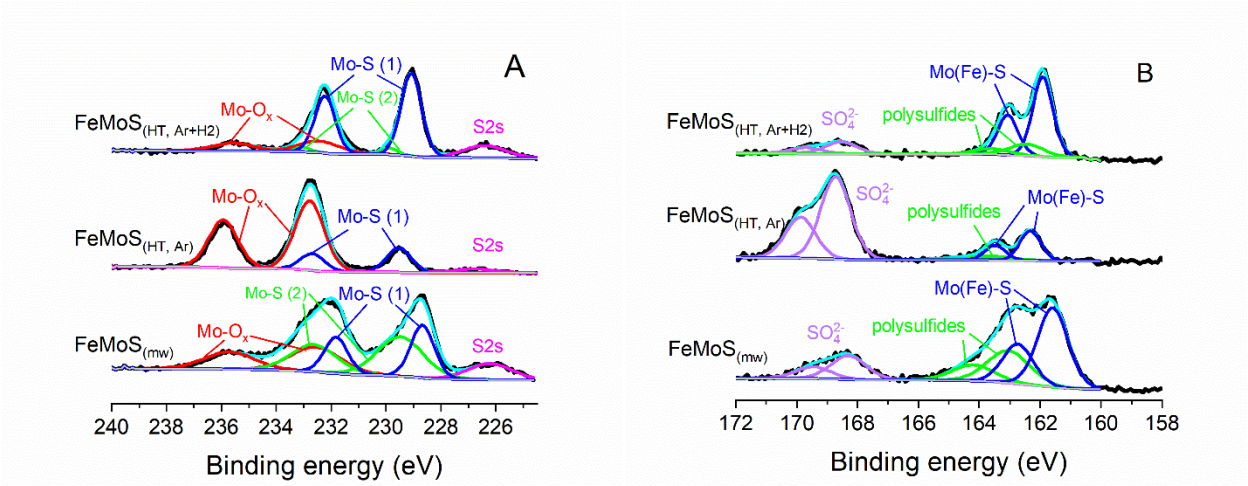


**Figure 5**. High resolution XPS spectra of (A) Mo3d and (B) S2p.

We finally estimated the electrochemical active surface area (ECSA) of the different materials by recording cyclic voltammograms of the as-synthesized materials drop-cast on glassy carbon electrodes in aqueous electrolyte and in the presence of $K_3[Fe(CN)_6]$ (SI, Figure S9, Table S1).[71-73] These measurements showed that microwave-synthesized amorphous materials have a larger electrochemical surface area and therefore expose more active sites toward the electrolyte compared to materials synthesized by heat treatment. The latter being more crystalline, indeed are only catalytically active at the edges sites.

*Hydrogen evolution electrocatalytic activity*

The electrochemical activity of these three materials towards the HER was investigated under aqueous acidic conditions (pH 0.3) relevant to PEM water electrolysis conditions using a static three-electrode configuration. We used the overpotential necessary (denoted as $\eta_{10}^{HER}$ in this work) to achieve a magnitude current density per geometric area $|j| = 10$ mA·cm$^{-2}$ as principal figure of merit of the HER activity. This value corresponds to the approximate current density expected for 10 % efficient solar-to-fuels conversion device under 1 sun illumination.[74-75]

The electrode formulation study has been carried out in order to evaluate a possible effect on the HER activity. Although $MoS_2$ is a promising catalyst, its low conductivity and low density of active sites have been identified as bottlenecks for efficient HER activity. Among the various strategies developed to overcome their low conductivity, the combination of $MoS_2$ with carbon materials leads to a clearly improved catalytic activity.[76-78] We therefore chose to use multi-walled carbon nanotubes (CNTs) as carbon conducting material and mixed them with our materials to evaluate their effect on its HER performances. As a control, the pristine $FeMoS_{(mw)}$ electrocatalyst was deposited onto a GDL substrate to achieve a catalyst loading of 0.24 mg·cm$^{-2}$ (Figure 6A, brown curve). In a second formulation, a CNTs layer was deposited onto GDL prior depositing the $FeMoS_{(mw)}$ catalytic layer (Figure 6A, yellow curve). The third strategy consisted of depositing a catalytic layer containing physically-mixed $FeMoS_{(mw)}$ and CNTs ($FeMoS_{(mw)}$:CNTs =5:1, mass ratio) in the prepared catalytic ink onto GDL (Figure 6A, purple curve). The SEM image of the catalytic ink (Figure 6C) shows a random network of CNTs bundles homogeneously distributed over the catalyst particles. The polarization curves of different electrodes (Figure 6A) reveal a large dependence of the performances on electrode formulation. The optimal electrode formulation was found to be physically-mixed $FeMoS_{(mw)}$ and CNTs in one catalytic layer. The presence of CNTs increases the surface, improves the poor

intrinsic conductivity[79] and optimizes active site availability and accessibility during HER catalysis throughout the $FeMoS_{(mw)}$ material. This three-dimensional architecture of the catalytic layer is favorable to a better catalyst accessibility and higher electrochemically active surface area, providing positive effects on HER performance. To quantify this effect, we calculated the double layer capacitances ($C_{DL}$) of our electrodes from cyclic voltammetry measurements (Figure S10). $C_{DL}$ values are directly proportional to the electrochemically active surface area (ECSA).[75] By adding CNTs, the $C_{DL}$ is more than eleven times higher than that of $FeMoS_{(mw)}$ without CNTs. Accordingly, the GDL/($FeMoS_{(mw)}$+CNTs) electrode displays a ca. 8-fold higher current density at −0.18 V vs RHE compared to GDL/$FeMoS_{(mw)}$ electrode without CNTs.

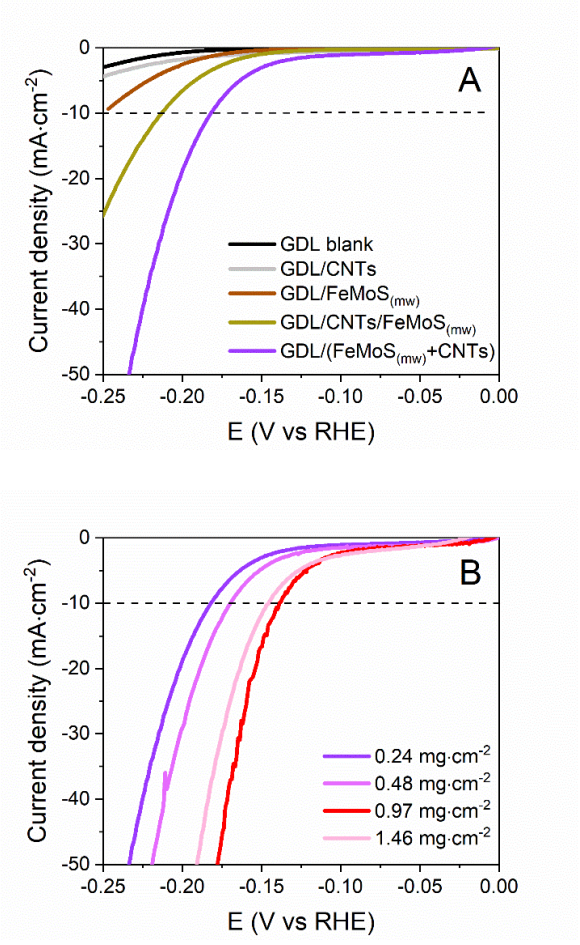

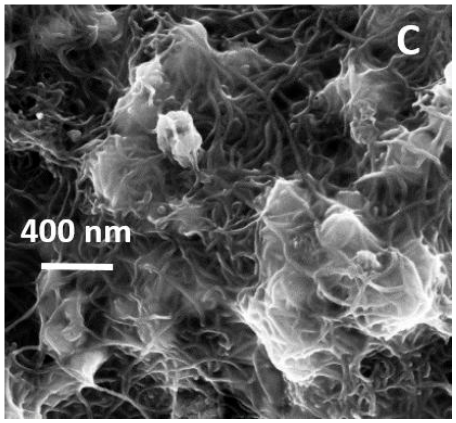


**Figure 6**. Polarization curves for HER corresponding to: (A) various electrode formulations with FeMoS(mw) electrocatalyst (catalyst loading 0.24 mg·cm–2 and CNTs loading 0.05 mg·cm–2); (B) GDL/(FeMoS(mw)+CNTs) with various catalyst loadings (mass ratio of catalyst to CNTs is 5:1). Conditions: N2-saturated 0.5 M H2SO4, scan rate 5 mV·s–1, Ti wire counter electrode. The blank curves (GDL and GDL/CNTs) are shown for comparison. (C) SEM image of (FeMoS(mw)+CNTs) catalytic ink.

As a second step, the electrode formulation was optimized for catalyst mass loading. The polarization curves from Figure 6B display the improvement in the HER activity when varying the catalyst loading from 0.24 mg·cm$^{-2}$ to 0.97 mg·cm$^{-2}$ (preserving the mass ratio of catalyst to CNTs at 5:1). As expected, a higher catalyst loading initially enhances the current density of the HER reaction. However, a slight decrease of the HER activity for catalyst loadings superior to 0.97 mg·cm$^{-2}$ was observed. This behavior is likely related to mass transfer limitations within the catalytic layer. Thus, the optimum catalyst loading for an optimal HER performance is a compromise between the number of active sites in the catalytic layer and mass transport of protons and hydrogen gas within this catalytic layer, which highly depends on its thickness.[80-82]

For comparison, the required overpotential ($\eta_{10}^{HER}$) to reach 10 mA·cm$^{-2}$ is 140 mV (Table 1) for the $FeMoS_{(mw)}$ electrocatalyst, thus 30 mV lower than that of the $MoS_{(mw)}$ electrocatalyst

($\eta_{10}^{HER}$ = 170 mV, Figure S11). This result indicates a concerted effect of Fe doping and Mo on the HER activity of bimetallic iron-molybdenum sulfide, as previously shown for Fe-$MoS_3$,[37] although the latter displays lower HER performance than $FeMoS_{(mw)}$. Performance parameters such as $\eta_{10}^{HER}$ and current density of our microwave synthesized molybdenum sulfide are in the range reported for most electrocatalysts of this type.[83]

The other two materials synthesized by heat treatment display poorer performances under similar conditions: both $FeMoS_{(HT,\ Ar)}$ and $FeMoS_{(HT,\ Ar+H_2)}$ display higher $\eta_{10}^{HER}$ values than $FeMoS_{(mw)}$, 206 mV and 180 mV, respectively (Figure 7A, Table 1). The higher overpotential requirement is likely related to the segregation of molybdenum- and iron-rich phases as evidenced by EDS mapping and to the presence of crystalline molybdenum sulfide (induced by the presence of Fe), which is known to be a poor HER catalyst compared to a-$MoS_x$.[84] As a consequence, both heat-treated (Fe, Mo)-sulfides display a higher $\eta_{10}^{HER}$ (Figure S12) compared to heat-treated Mo-sulfides ($\eta_{10}^{HER} \sim$ 160 mV).

The kinetics study and mechanistic pathway for HER were examined using Tafel plots derived from polarization curves of synthesized (Fe, Mo)-sulfides (Figure 7B). These slopes are related to multistep electrochemical reactions occurring at the catalyst surface during HER and thus can be used as a signature of the HER mechanism. As generally accepted, Tafel slopes of 120, 30 and 40 $mV \cdot dec^{-1}$ reveal Volmer, Tafel and Heyrovsky rate-determining step (*rds*), respectively.[85-87] The $FeMoS_{(mw)}$ electrocatalyst has the lowest Tafel slope value (57 $mV \cdot dec^{-1}$, Table 1) in the as-prepared electrode, GDL/($FeMoS_{(mw)}$+CNTs). Tafel slopes of $FeMoS_{(HT,\ Ar)}$ and $FeMoS_{(HT,\ Ar+H_2)}$ are 126 $mV \cdot dec^{-1}$ and 101 $mV \cdot dec^{-1}$, respectively (Table 1). The smallest Tafel value for $FeMoS_{(mw)}$ suggests faster kinetics which corresponds with its higher electrocatalytic activity for HER (lower $\eta_{10}^{HER}$) compared with the other two (Fe, Mo)-sulfides.

Considering the experimental value (57 mV·dec$^{-1}$) a Volmer-Heyrovsky mechanism is proposed with a Heyrovsky reaction or an intermediate diffusion step of adsorbed hydrogen atoms as *rds*.[88-90] This conclusion is in line with the data previously reported for electrodeposited Fe-$MoS_3$ films.[37]

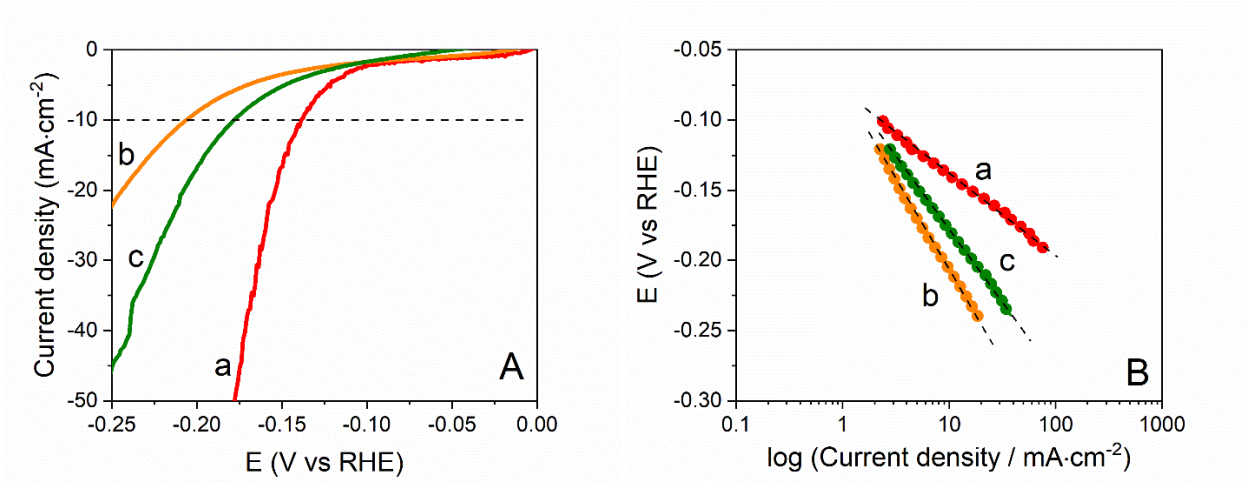


**Figure 7**. Polarization curves (A) and Tafel plots (B) for HER on: (a). GDL/($FeMoS_{(mw)}$+CNTs), (b). GDL/($FeMoS_{(HT,\ Ar)}$+CNTs) and (c). GDL/($FeMoS_{(HT,\ Ar+H_2)}$+CNTs); ($N_2$-saturated 0.5 M $H_2SO_4$, scan rate 5 mV·s$^{-1}$, Ti wire counter electrode, catalyst loading 0.97 mg·cm$^{-2}$).

It thus appears that the addition of iron significantly improves the HER activity (Figure S11) of amorphous material obtained via the microwave synthetic approach. Although the reasons for such enhancement are still undefined at a molecular level, this observation is in line with previous studies about such amorphous materials.[37, 91] By contrast, addition of iron negatively impacts the HER performances of the heat treated materials, likely because it induces the crystallization of the molybdenum sulfide phase and reduces the ECSA (Table S1).

As a result of this study is thus $FeMoS_{(mw)}$ is found to be the most promising catalyst for further development: itt evolves $H_2$ with the lowest $\eta_{10}^{HER}$ value, smallest Tafel slope and with a 100 % faradic efficiency as determined during chronoamperometry measurements at −160 mV

vs RHE for 4 h (Figure 8A). In order to investigate its potential for technological application, the stability of this material upon HER turnover was analysed. Chronopotentiometry (CP) was performed for 70 h at a current density of –10 mA·cm$^{-2}$ (Figure 8B). Only a slight increase (ca. 30 mV) in $\eta_{10}^{HER}$ was observed over 70 h, with a plateau after 24 h, therefore showing the high stability of the GDL/(FeMoS$_{(mw)}$+CNTs) electrode under operation.

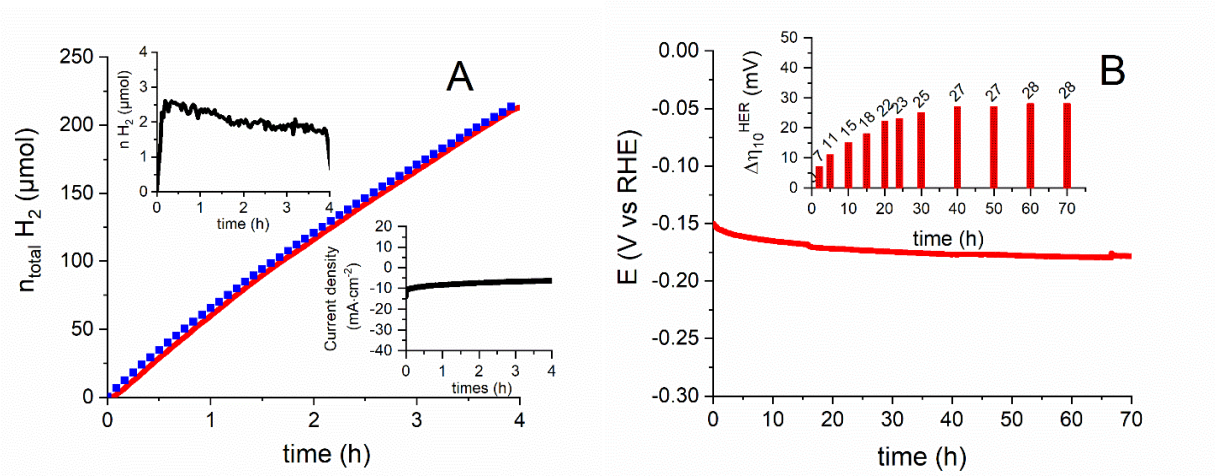


**Figure 8.** (A). Chronoamperometry measurements (amount of hydrogen produced assuming a unity faradaic efficiency (blue square) and as observed by the in-line gas chromatography setup (red line)) and (B). Chronopotentiometry measurements (insight graph: overpotential evolution ($\Delta\eta_{10}^{HER}$ /mV = $\eta_{10}^{HER}$ (t)/mV–$\eta$(t$_0$)/mV) during 70 h operation) on GDL/(FeMoS$_{(mw)}$+CNTs) electrode. ($N_2$-saturated 0.5 M $H_2SO_4$, Ti wire counter electrode, catalyst loading 0.97 mg·cm$^{-2}$).

*PEM electrolyzer testing*

For the technological implementation of our catalyst, Vulcan was selected for the electrode fabrication in PEM electrolyzer (SI, Figure S13). Vulcan is indeed the most widely used support in the PEM fuel cells and electrolyzer applications due to their properties, commercial availability and low cost.[92-93] Electrolysis tests were performed in a 5 cm$^2$ PEM electrolyzer single cell (Scribner) at 80 °C or RT.

Different MEAs were prepared using ($FeMoS_{(mw)}$+Vulcan) (4 mg·cm$^{-2}$, catalyst:Vulcan = 1:1 mass ratio, Nafion-to-(catalyst+Vulcan) ratio of 1.4) or Pt-C (0.5 mg·cm$^{-2}$) as the HER catalysts, commercial Ir black (2 mg·cm$^{-2}$) as the OER catalyst and Nafion NRE-212 membrane (50 μm thick) as polymer electrolyte membrane. MEAs were prepared by hot pressing. The OER catalyst was deposited onto the anode side of the membrane through the decal method of deposition and the HER catalyst was deposited by drop-cast onto a GDL.

The polarization curves of the measured MEAs are shown in Figure 9. In spite of a smaller efficiency of Ir/($FeMoS_{(mw)}$+Vulcan) electrolyzer than that of Ir/Pt-C electrolyzer, notable electrochemical performances are obtained. At 80 °C (Table S2) the performance achieved with Ir/($FeMoS_{(mw)}$+Vulcan) electrolyzer was 0.5 A·cm$^{-2}$ at 1.77 V and 1 A·cm$^{-2}$ at 1.85 V. For comparison, Ir/Pt-C electrolyzer requires 1.5 V to reach 0.5 A·cm$^{-2}$ and 1.54 V to reach 1 A·cm$^{-2}$. This electrocatalytic activity is strongly temperature dependent (Figure S14), with Ir/($FeMoS_{(mw)}$+Vulcan) electrolyzer reaching 0.5 A·cm$^{-2}$ at 1.93 V at RT. For comparison, Ir/Pt-C electrolyzer requires 1.62 V to reach 0.5 A·cm$^{-2}$ at RT.

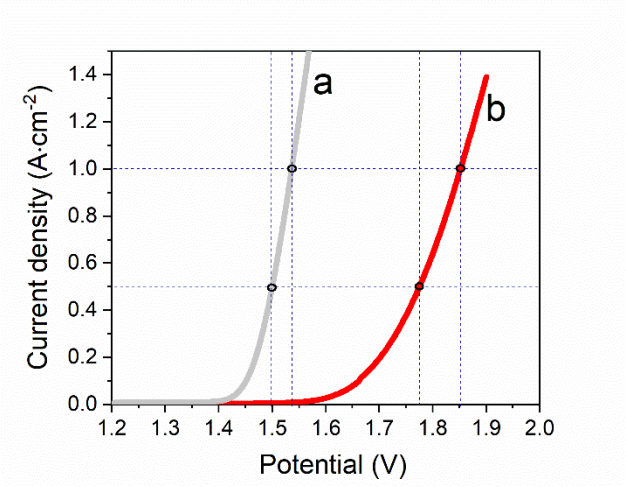


**Figure 9**. Single cell polarization curves for PEM electrolysis at 80 °C using two distinct MEA: (a). Ir black/NRE-212/Pt-C and (b). Ir black/NRE-212/($FeMoS_{(mw)}$+Vulcan).

An in-situ accelerated stress test (AST) was then carried out to assess the durability of the MEA. Standardized AST protocols are well developed for PEM fuel cell technology[94-96] while the establishment of standardized AST protocols for PEM water electrolysis is still under development.[97] We exploit here an AST protocol for a quick (over 24 h) evaluation of the MEA durability, adapted from the work performed in the NOVEL EU Project.[98] The AST is continuously applied for 24 h. The method involves cycling between 0.05 $A{\cdot}cm^{-1}$ minimum intensity and 0.5 $A{\cdot}cm^{-1}$ maximum intensity with each intensity value being maintained for 15 min (Figure 10A, Figure S15). The voltage required to reach 0.5 $A{\cdot}cm^{-2}$ before and after AST is shown in Figure 10B and Figure S16. Both electrolyzers (Ir/($FeMoS_{(mw)}$+Vulcan) and Ir/Pt-C) exhibit a very good and similar stability under the testing conditions with a gradual increase in potential over the 24 h test period. After 24 h AST, Ir/($FeMoS_{(mw)}$+Vulcan) electrolyzer required an additional 45 mV to reach 0.5 $A{\cdot}cm^{-2}$ (40 mV for Ir/Pt-C electrolyzer). Similar behavior was observed in the polarization curves before and after AST (Figure 10C). The degradation slopes (in $\mu V{\cdot}h^{-1}$) calculated from AST measurement are shown in Figure 10D. At higher current

density, a smaller difference between Ir/Pt-C and Ir/($FeMoS_{(mw)}$+Vulcan) electrolyzers was obtained.

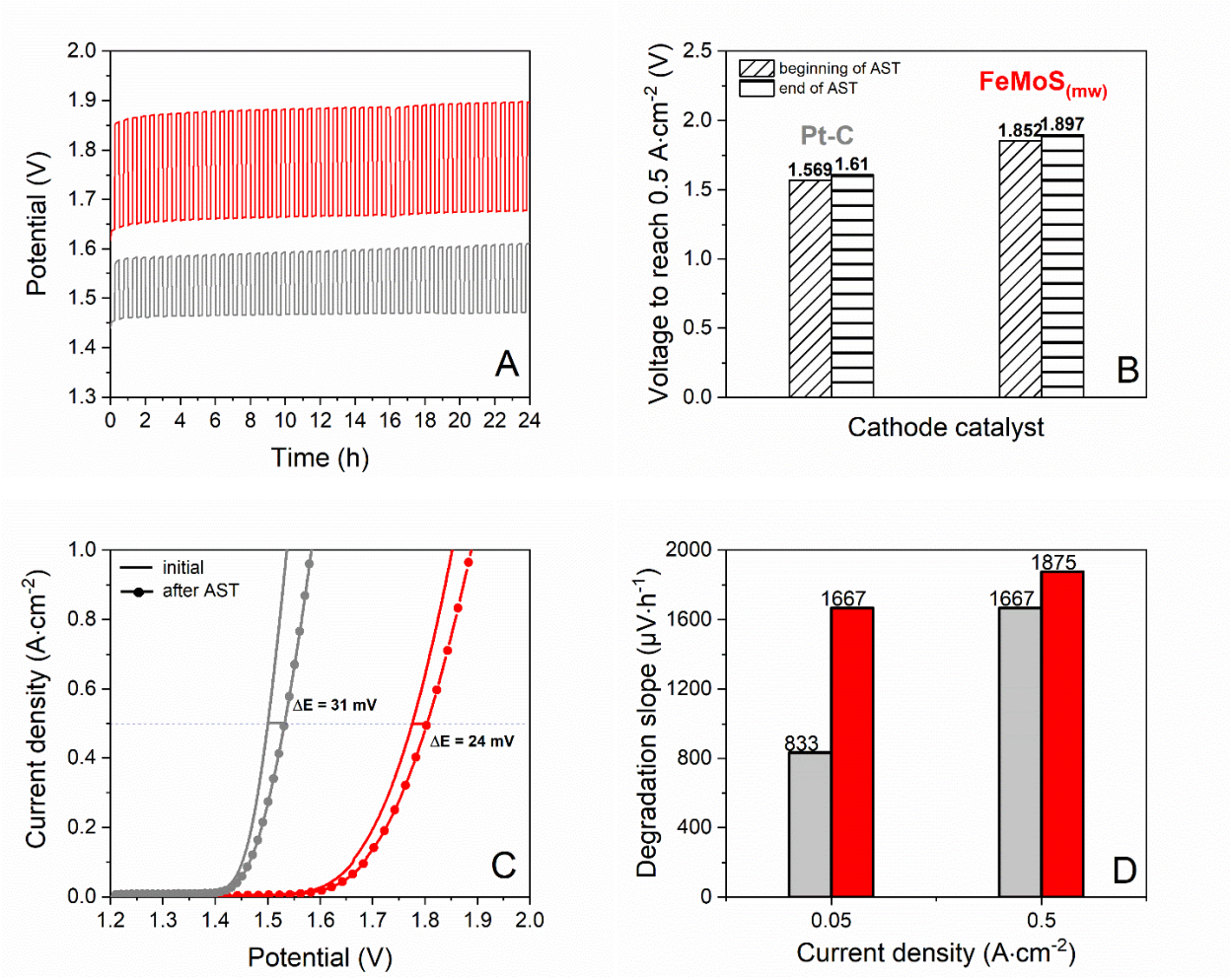


**Figure 10**. Performances of PEM electrolyzers (80 °C) with Pt-C (0.5 mg·cm$^{-2}$, in gray) or ($FeMoS_{(mw)}$+Vulcan) (4 mg·cm$^{-2}$, in red) as HER catalysts and Ir black (2 mg·cm$^{-2}$) as OER catalyst. (A) AST carried out for 24 h, (B). Comparison of the voltage required to reach 0.5 A·cm$^{-2}$ (from AST measurement), (C). Polarization curves before and after AST, (D). Degradation slope during AST.

To the best of our knowledge, there is no any other report of bimetallic sulfides such as M-Mo-S (where M is Fe or other abundant metal) integrated as HER catalyst into PEM electrolyzers.

Performances have been reported for Mo-based catalysts (mixed with various forms of carbon)-based PEM electrolyzer working at 80 °C (from 0.1 to 0.5 $A \cdot cm^{-2}$ at ca. 1.9 V)[41-42] and at 45 °C in a flow-cell setup (0.3 $A \cdot cm^{-2}$ at 2 V).[43] Additionally, under similar operating conditions (e.g. 80 °C) a current density of ca. 0.5 $A \cdot cm^{-2}$ was reached at 2 V with a $FeS_2$-Vulcan cathode catalyst.[45] Our bimetallic (Fe, Mo)-sulfide catalyst, $FeMoS_{(mw)}$, outperforms the current metal sulfide catalysts implemented in PEM electrolyzers, and is thus promising for commercial application. With the $FeMoS_{(mw)}$ we report lower potential to reach the same current density compared to previously reported $MoS_2$-based or $FeS_2$-based PEM cathodes (Table S2).

## CONCLUSIONS

Developing inexpensive, stable and efficient catalysts for HER is of great importance to replace scarce and costly platinum-based catalysts to make the electrolysis process for renewable hydrogen production economically feasible. This work provides scalable approaches for designing bimetallic iron-molybdenum sulfide electrocatalysts for HER. The synthetic method, microwave irradiation and heat treatment, respectively, directly impacts the structure and composition of materials. The low amounts iron incorporated in the microwave synthetic approach promote the HER performance of the amorphous $FeMoS_{(mw)}$. The higher amounts of iron incorporated in crystalline structures by contrast impedes the catalytic HER activity of the catalysts obtained by heat treatment. Combined with carbon materials (CNTs, Vulcan), these electrocatalysts show high activity towards the HER in acidic media, which allows to implement them as cathode catalyst into a PEM electrolyzer single cell. These new noble-metal free materials require only ca. 300 mV additional voltage compared to Pt-catalyst, and show similar stability under operation. Future study will be devoted to the coupling of such materials with

PEM-compatible oxygen evolution reaction (OER) catalysts based on Earth-abundant elements.[99-100]

ASSOCIATED CONTENT

**Supporting Information**. **Supporting Information.** Additional experimental details, PEM electrolyzer setup, SEM images, Raman spectra, XPS spectra, electrochemical results (PDF).

AUTHOR INFORMATION

**Corresponding Author**

* Vincent Artero - Univ. Grenoble Alpes, CNRS, CEA/IRIG, Laboratoire de Chimie et Biologie des Métaux, 17 rue des Martyrs, 38054 Grenoble, France

E-mail: vincent.artero@cea.fr

**Present Addresses**

Camille Roiron: Univ. Grenoble Alpes, CEA, LITEN/DEHT, 17 rue des Martyrs 38054 Grenoble, France

**Author Contributions**

The manuscript was written through contributions of all authors. All authors have given approval to the final version of the manuscript. #These authors contributed equally.

ACKNOWLEDGMENT

The authors gratefully acknowledge the French National Research Agency (Labex ARCANE, CBH-EUR-GS, ANR-17-EURE-0003), the European Research Council and European

Commission's Horizon 2020 research and innovation program (grant agreement No 836429, project PRODUCE-H2).

REFERENCES

(1) Gielen, D.; Boshell, F.; Saygin, D.; Bazilian, M. D.; Wagner, N.; Gorini, R., The role of renewable energy in the global energy transformation. *Energy Strateg. Rev.* **2019,** *24*, 38-50.

(2) Staffell, I.; Scamman, D.; Velazquez Abad, A.; Balcombe, P.; Dodds, P. E.; Ekins, P.; Shah, N.; Ward, K. R., The role of hydrogen and fuel cells in the global energy system. *Energy Environ. Sci.* **2019,** *12* (2), 463-491.

(3) Parra, D.; Valverde, L.; Pino, F. J.; Patel, M. K., A review on the role, cost and value of hydrogen energy systems for deep decarbonisation. *Renew. Sust. Energ. Rev.* **2019,** *101*, 279-294.

(4) Hydrogen scaling up (A sustainable pathway for the global energy transition).

(5) Guandalini, G.; Campanari, S.; Valenti, G., Comparative assessment and safety issues in state-of-the-art hydrogen production technologies. *Int. J. Hydrogen Energy* **2016,** *41* (42), 18901-18920.

(6) Dawood, F.; Anda, M.; Shafiullah, G. M., Hydrogen production for energy: An overview. *Int. J. Hydrogen Energy* **2020,** *45* (7), 3847-3869.

(7) Shiva Kumar, S.; Himabindu, V., Hydrogen production by PEM water electrolysis – A review. *Mater. Sci. .Energy Technol.* **2019,** *2* (3), 442-454.

(8) Barbir, F., PEM electrolysis for production of hydrogen from renewable energy sources. *Sol. Energy* **2005,** *78* (5), 661-669.

(9) Schiller, G.; Henne, R.; Mohr, P.; Peinecke, V., High performance electrodes for an advanced intermittently operated 10-kW alkaline water electrolyzer. *Int. J. Hydrogen Energy* **1998,** *23* (9), 761-765.

(10) Zeng, K.; Zhang, D., Recent progress in alkaline water electrolysis for hydrogen production and applications. *Prog. Energy Combust. Sci.* **2010,** *36* (3), 307-326.

(11) Saba, S. M.; Müller, M.; Robinius, M.; Stolten, D., The investment costs of electrolysis – A comparison of cost studies from the past 30 years. *Int. J. Hydrogen Energy* **2018,** *43* (3), 1209-1223.

(12) Miller, H. A.; Bouzek, K.; Hnat, J.; Loos, S.; Bernäcker, C. I.; Weißgärber, T.; Röntzsch, L.; Meier-Haack, J., Green hydrogen from anion exchange membrane water electrolysis: a review of recent developments in critical materials and operating conditions. *Sustainable Energy Fuels* **2020,** *4* (5), 2114-2133.

(13) Carmo, M.; Fritz, D. L.; Mergel, J.; Stolten, D., A comprehensive review on PEM water electrolysis. *Int. J. Hydrogen Energy* **2013,** *38* (12), 4901-4934.

(14) Babic, U.; Suermann, M.; Büchi, F. N.; Gubler, L.; Schmidt, T. J., Critical Review—Identifying Critical Gaps for Polymer Electrolyte Water Electrolysis Development. *J. Electrochem. Soc.* **2017,** *164* (4), F387-F399.

(15) Ayers, K., The potential of proton exchange membrane–based electrolysis technology. *Curr. Opin. Electrochem.* **2019,** *18*, 9-15.

(16) Schmidt, O.; Gambhir, A.; Staffell, I.; Hawkes, A.; Nelson, J.; Few, S., Future cost and performance of water electrolysis: An expert elicitation study. *Int. J. Hydrogen Energy* **2017,** *42* (52), 30470-30492.

(17) Grigoriev, S. A.; Porembsky, V. I.; Fateev, V. N., Pure hydrogen production by PEM electrolysis for hydrogen energy. *Int. J. Hydrogen Energy* **2006,** *31* (2), 171-175.

(18) Klose, C.; Trinke, P.; Böhm, T.; Bensmann, B.; Vierrath, S.; Hanke-Rauschenbach, R.; Thiele, S., Membrane interlayer with Pt recombination particles for reduction of the anodic hydrogen content in PEM water electrolysis. *J. Electrochem. Soc.* **2018,** *165* (16), F1271-F1277.

(19) Rozain, C.; Mayousse, E.; Guillet, N.; Millet, P., Influence of iridium oxide loadings on the performance of PEM water electrolysis cells: Part I–pure $IrO_2$-based anodes. *Appl. Catal. B: Environ.* **2016,** *182*, 153-160.

(20) Liu, B.; Wang, C.; Chen, Y., Surface determination and electrochemical behavior of $IrO_2$-$RuO_2$-$SiO_2$ ternary oxide coatings in oxygen evolution reaction application. *Electrochim. Acta* **2018,** *264*, 350-357.

(21) Gordon, R. B.; Bertram, M.; Graedel, T. E., Metal stocks and sustainability. *Proc. Natl. Acad. Sci. U.S.A* **2006,** *103* (5), 1209.

(22) Esposito, D. V., Membraneless electrolyzers for low-cost hydrogen production in a renewable energy future. *Joule* **2017,** *1* (4), 651-658.

(23) Evans, D. J.; Pickett, C. J., Chemistry and the hydrogenases. *Chem. Soc. Rev.* **2003,** *32* (5), 268-275.

(24) Lee, S. C.; Holm, R. H., Speculative synthetic chemistry and the nitrogenase problem. *Proc. Nat. Acad. Sci. U.S.A.* **2003,** *100* (7), 3595-3600.

(25) Tributsch, H.; Bennett, J. C., Electrochemistry and photochemistry of MoS2 layer crystals. 1. *J. Electroanal. Chem.* **1977,** *81* (1), 97-111.

(26) Hinnemann, B.; Moses, P. G.; Bonde, J.; Jørgensen, K. P.; Nielsen, J. H.; Horch, S.; Chorkendorff, I.; Nørskov, J. K., Biomimetic hydrogen evolution: $MoS_2$ nanoparticles as catalyst for hydrogen evolution. *J. Am. Chem. Soc.* **2005,** *127* (15), 5308-5309.

(27) Jaramillo, T. F.; Jørgensen, K. P.; Bonde, J.; Nielsen, J. H.; Horch, S.; Chorkendorff, I., Identification of active edge sites for electrochemical $H_2$ evolution from $MoS_2$ nanocatalysts. *Science* **2007,** *317* (5834), 100.

(28) Anantharaj, S.; Ede, S. R.; Sakthikumar, K.; Karthick, K.; Mishra, S.; Kundu, S., Recent trends and perspectives in electrochemical water splitting with an emphasis on sulfide, selenide, and phosphide catalysts of Fe, Co, and Ni: a review. *ACS Catal.* **2016,** *6* (12), 8069-8097.

(29) Zou, X.; Zhang, Y., Noble metal-free hydrogen evolution catalysts for water splitting. *Chem. Soc. Rev.* **2015,** *44* (15), 5148-5180.

(30) Zhang, J.; Bai, X.; Wang, T.; Xiao, W.; Xi, P.; Wang, J.; Gao, D.; Wang, J., Bimetallic nickel cobalt sulfide as efficient electrocatalyst for Zn-air battery and water splitting. *Nanomicro Lett* **2019,** *11* (1), 2-2.

(31) Wang, D.-Y.; Gong, M.; Chou, H.-L.; Pan, C.-J.; Chen, H.-A.; Wu, Y.; Lin, M.-C.; Guan, M.; Yang, J.; Chen, C.-W.; Wang, Y.-L.; Hwang, B.-J.; Chen, C.-C.; Dai, H., Highly active and

stable hybrid catalyst of cobalt-doped $FeS_2$ nanosheets–carbon nanotubes for hydrogen evolution reaction. *J. Am. Chem. Soc.* **2015,** *137* (4), 1587-1592.

(32) Miao, J.; Xiao, F.-X.; Yang, H. B.; Khoo, S. Y.; Chen, J.; Fan, Z.; Hsu, Y.-Y.; Chen, H. M.; Zhang, H.; Liu, B., Hierarchical Ni-Mo-S nanosheets on carbon fiber cloth: A flexible electrode for efficient hydrogen generation in neutral electrolyte. *Sci. Adv.* **2015,** *1* (7), e1500259.

(33) Zhu, H.; Zhang, J.; Yanzhang, R.; Du, M.; Wang, Q.; Gao, G.; Wu, J.; Wu, G.; Zhang, M.; Liu, B.; Yao, J.; Zhang, X., When cubic cobalt sulfide meets layered molybdenum disulfide: a core–shell system toward synergetic electrocatalytic water splitting. *Adv. Mater.* **2015,** *27* (32), 4752-4759.

(34) Bonde, J.; Moses, P. G.; Jaramillo, T. F.; Nørskov, J. K.; Chorkendorff, I., Hydrogen evolution on nano-particulate transition metal sulfides. *Faraday Discuss.* **2009,** *140* (0), 219-231.

(35) Bolar, S.; Shit, S.; Kumar, J. S.; Murmu, N. C.; Ganesh, R. S.; Inokawa, H.; Kuila, T., Optimization of active surface area of flower like $MoS_2$ using V-doping towards enhanced hydrogen evolution reaction in acidic and basic medium. *Appl. Catal. B: Environ.* **2019,** *254*, 432-442.

(36) Shi, Y.; Zhou, Y.; Yang, D.-R.; Xu, W.-X.; Wang, C.; Wang, F.-B.; Xu, J.-J.; Xia, X.-H.; Chen, H.-Y., Energy level engineering of $MoS_2$ by transition-metal doping for accelerating hydrogen evolution reaction. *J. Am. Chem. Soc.* **2017,** *139* (43), 15479-15485.

(37) Merki, D.; Vrubel, H.; Rovelli, L.; Fierro, S.; Hu, X., Fe, Co, and Ni ions promote the catalytic activity of amorphous molybdenum sulfide films for hydrogen evolution. *Chem. Sci.* **2012,** *3* (8), 2515-2525.

(38) Zhao, X.; Ma, X.; Lu, Q.; Li, Q.; Han, C.; Xing, Z.; Yang, X., $FeS_2$-doped $MoS_2$ nanoflower with the dominant 1T-$MoS_2$ phase as an excellent electrocatalyst for high-performance hydrogen evolution. *Electrochim. Acta* **2017,** *249*, 72-78.

(39) Ren, X.; Wang, W.; Ge, R.; Hao, S.; Qu, F.; Du, G.; Asiri, A. M.; Wei, Q.; Chen, L.; Sun, X., An amorphous $FeMoS_4$ nanorod array toward efficient hydrogen evolution electrocatalysis under neutral conditions. *Chem. Commun.* **2017,** *53* (64), 9000-9003.

(40) Sun, X.; Xu, K.; Fleischer, C.; Liu, X.; Grandcolas, M.; Strandbakke, R.; Bjørheim, T. S.; Norby, T.; Chatzitakis, A., Earth-abundant electrocatalysts in proton exchange membrane electrolyzers. *Catalysts* **2018,** *8* (12), 657.

(41) Corrales-Sánchez, T.; Ampurdanés, J.; Urakawa, A., $MoS_2$-based materials as alternative cathode catalyst for PEM electrolysis. *Int. J. Hydrogen Energy* **2014,** *39* (35), 20837-20843.

(42) Ng, J. W. D.; Hellstern, T. R.; Kibsgaard, J.; Hinckley, A. C.; Benck, J. D.; Jaramillo, T. F., Polymer electrolyte membrane electrolyzers utilizing non-precious Mo-based hydrogen evolution catalysts. *ChemSusChem* **2015,** *8* (20), 3512-3519.

(43) Lu, A.-Y.; Yang, X.; Tseng, C.-C.; Min, S.; Lin, S.-H.; Hsu, C.-L.; Li, H.; Idriss, H.; Kuo, J.-L.; Huang, K.-W.; Li, L.-J., High-sulfur-vacancy amorphous molybdenum sulfide as a high current electrocatalyst in hydrogen evolution. *Small* **2016,** *12* (40), 5530-5537.

(44) Kim, J. H.; Kim, H.; Kim, J.; Lee, H. J.; Jang, J. H.; Ahn, S. H., Electrodeposited molybdenum sulfide as a cathode for proton exchange membrane water electrolyzer. *J. Power Sources* **2018,** *392*, 69-78.

(45) Giovanni, C. D.; Reyes-Carmona, Á.; Coursier, A.; Nowak, S.; Grenèche, J. M.; Lecoq, H.; Mouton, L.; Rozière, J.; Jones, D.; Peron, J.; Giraud, M.; Tard, C., Low-cost nanostructured iron sulfide electrocatalysts for PEM water electrolysis. *ACS Catal.* **2016,** *6* (4), 2626-2631.

(46) Reuillard, B.; Blanco, M.; Calvillo, L.; Coutard, N.; Ghedjatti, A.; Chenevier, P.; Agnoli, S.; Otyepka, M.; Granozzi, G.; Artero, V., Noncovalent integration of a bioinspired Ni catalyst to graphene acid for reversible electrocatalytic hydrogen oxidation. *ACS Appl. Mater. Interfaces* **2020,** *12* (5), 5805-5811.

(47) O'Reilly, J. E., Oxidation-reduction potential of the ferro-ferricyanide system in buffer solutions. *Biochim. Biophys. Acta, Bioenerg.* **1973,** *292* (3), 509-515.

(48) Cobo, S.; Heidkamp, J.; Jacques, P. A.; Fize, J.; Fourmond, V.; Guetaz, L.; Jousselme, B.; Ivanova, V.; Dau, H.; Palacin, S.; Fontecave, M.; Artero, V., A Janus cobalt-based catalytic material for electro-splitting of water. *Nat. Mater.* **2012,** *11* (9), 802-807.

(49) Ge, J.; Higier, A.; Liu, H., Effect of gas diffusion layer compression on PEM fuel cell performance. *J. Power Sources* **2006,** *159* (2), 922-927.

(50) Chen, D.; Tang, K.; Shen, G.; Sheng, J.; Fang, Z.; Liu, X.; Zheng, H.; Qian, Y., Microwave-assisted synthesis of metal sulfides in ethylene glycol. *Mater. Chem. Phys.* **2003,** *82* (1), 206-209.

(51) Yu, S.-H.; Shu, L.; Yang, J.; Han, Z.-H.; Qian, Y.-T.; Zhang, Y.-H., A solvothermal decomposition process for fabrication and particle sizes control of $Bi_2S_3$ nanowires. *J. Mater. Res.* **2011,** *14* (11), 4157-4162.

(52) Tran, P. D.; Tran, T. V.; Orio, M.; Torelli, S.; Truong, Q. D.; Nayuki, K.; Sasaki, Y.; Chiam, S. Y.; Yi, R.; Honma, I.; Barber, J.; Artero, V., Coordination polymer structure and revisited hydrogen evolution catalytic mechanism for amorphous molybdenum sulfide. *Nat. Mater.* **2016,** *15* (6), 640-647.

(53) Li, Y.; Yu, Y.; Huang, Y.; Nielsen, R. A.; Goddard, W. A.; Li, Y.; Cao, L., Engineering the composition and crystallinity of molybdenum sulfide for high-performance electrocatalytic hydrogen evolution. *ACS Catal.* **2015,** *5* (1), 448-455.

(54) Pham, K.-C.; McPhail, D. S.; Wee, A. T. S.; Chua, D. H. C., Amorphous molybdenum sulfide on graphene–carbon nanotube hybrids as supercapacitor electrode materials. *RSC Adv.* **2017,** *7* (12), 6856-6864.

(55) Dinda, D.; Ahmed, M. E.; Mandal, S.; Mondal, B.; Saha, S. K., Amorphous molybdenum sulfide quantum dots: an efficient hydrogen evolution electrocatalyst in neutral medium. *J. Mater. Chem. A* **2016,** *4* (40), 15486-15493.

(56) Duan, Y.; Liu, Y.; Chen, Z.; Liu, D.; Yu, E.; Zhang, X.; Fu, H.; Fu, J.; Zhang, J.; Du, H., Amorphous molybdenum sulfide nanocatalysts simultaneously realizing efficient upgrading of residue and synergistic synthesis of 2D $MoS_2$ nanosheets/carbon hierarchical structures. *Green Chem.* **2020,** *22* (1), 44-53.

(57) Hai, X.; Zhou, W.; Chang, K.; Pang, H.; Liu, H.; Shi, L.; Ichihara, F.; Ye, J., Engineering the crystallinity of $MoS_2$ monolayers for highly efficient solar hydrogen production. *J. Mater. Chem. A* **2017,** *5* (18), 8591-8598.

(58) Nguyen, D. N.; Nguyen, L. N.; Nguyen, P. D.; Thu, T. V.; Nguyen, A. D.; Tran, P. D., Crystallization of amorphous molybdenum sulfide induced by electron or laser beam and its effect on $H_2$-evolving activities. *J. Phys. Chem. C* **2016,** *120* (50), 28789-28794.

(59) Kong, D.; Cha, J. J.; Wang, H.; Lee, H. R.; Cui, Y., First-row transition metal dichalcogenide catalysts for hydrogen evolution reaction. *Energy Environ. Sci.* **2013,** *6* (12), 3553-3558.

(60) Guo, X.; Wang, Z.; Zhu, W.; Yang, H., The novel and facile preparation of multilayer $MoS_2$ crystals by a chelation-assisted sol–gel method and their electrochemical performance. *RSC Adv.* **2017,** *7* (15), 9009-9014.

(61) Li, Y.; Nakamura, R., Structural change of molybdenum sulfide facilitates the electrocatalytic hydrogen evolution reaction at neutral pH as revealed by in situ Raman spectroscopy. *Chinese J. Catal.* **2018,** *39* (3), 401-406.

(62) Khai, T. V.; Long, L. N.; Phong, M. T.; Kien, P. T.; Thang, L. V.; Lam, T. D., Synthesis and optical properties of $MoS_2$/graphene nanocomposite. *J. Electron. Mater.* **2020,** *49* (2), 969-979.

(63) Sun, Z.; Yang, M.; Wang, Y.; Hu, Y. H., Novel binder-free three-dimensional $MoS_2$-based electrode for efficient and stable electrocatalytic hydrogen evolution. *ACS Appl. Energy Mater.* **2019,** *2* (2), 1102-1110.

(64) Alemán-Vázquez, L. O.; Torres-García, E.; Villagómez-Ibarra, J. R.; Cano-Domínguez, J. L., Effect of the particle size on the activity of $MoO_xC_y$ catalysts for the isomerization of heptane. *Catal. Lett.* **2005,** *100* (3), 219-226.

(65) Hao, Z.; Yang, S.; Niu, J.; Fang, Z.; Liu, L.; Dong, Q.; Song, S.; Zhao, Y., A bimetallic oxide $Fe_{1.89}Mo_{4.11}O_7$ electrocatalyst with highly efficient hydrogen evolution reaction activity in alkaline and acidic media. *Chem. Sci.* **2018,** *9* (25), 5640-5645.

(66) Zhang, W.; Shi, S.; Zhu, W.; Yang, C.; Li, S.; Liu, X.; Hu, N.; Huang, L.; Wang, R.; Suo, Y.; Li, Z.; Wang, J., In-Situ Fixation of All-Inorganic Mo–Fe–S Clusters for the Highly Selective Removal of Lead(II). *ACS App. Mater. Interfaces* **2017,** *9* (38), 32720-32726.

(67) Di Giovanni, C.; Wang, W.-A.; Nowak, S.; Grenèche, J.-M.; Lecoq, H.; Mouton, L.; Giraud, M.; Tard, C., Bioinspired iron sulfide nanoparticles for cheap and long-lived electrocatalytic molecular hydrogen evolution in neutral water. *ACS Catal.* **2014,** *4* (2), 681-687.

(68) Colomban, P.; Slodczyk, A., Raman Intensity: An important tool in the study of nanomaterials and nanostructures. *Acta Phys. Pol., A* **2009,** *116* (1), 7-12.

(69) Zhang, J.; Zhao, L.; Liu, A.; Li, X.; Wu, H.; Lu, C., Three-dimensional $MoS_2$/rGO hydrogel with extremely high double-layer capacitance as active catalyst for hydrogen evolution reaction. *Electrochim. Acta* **2015,** *182*, 652-658.

(70) Biesinger, M. C.; Payne, B. P.; Grosvenor, A. P.; Lau, L. W. M.; Gerson, A. R.; Smart, R. S. C., Resolving surface chemical states in XPS analysis of first row transition metals, oxides and hydroxides: Cr, Mn, Fe, Co and Ni. *Appl. Surf. Sci.* **2011,** *257* (7), 2717-2730.

(71) Song, M.-J.; Hwang, S. W.; Whang, D., Non-enzymatic electrochemical CuO nanoflowers sensor for hydrogen peroxide detection. *Talanta* **2010,** *80* (5), 1648-1652.

(72) Krejci, J.; Sajdlova, Z.; Nedela, V.; Flodrova, E.; Sejnohova, R.; Vranova, H.; Plicka, R., Effective surface area of electrochemical sensors. *J. Electrochem. Soc.* **2014,** *161* (6), B147-B150.

(73) Ameur, Z. O.; Husein, M. M., Electrochemical behavior of potassium ferricyanide in aqueous and (w/o) microemulsion systems in the presence of dispersed nickel nanoparticles. *Sep. Sci. Technol.* **2013,** *48* (5), 681-689.

(74) Walter, M. G.; Warren, E. L.; McKone, J. R.; Boettcher, S. W.; Mi, Q.; Santori, E. A.; Lewis, N. S., Solar water splitting cells. *Chem. Rev.* **2010,** *110* (11), 6446-6473.

(75) McCrory, C. C. L.; Jung, S.; Ferrer, I. M.; Chatman, S. M.; Peters, J. C.; Jaramillo, T. F., Benchmarking hydrogen evolving reaction and oxygen evolving reaction electrocatalysts for solar water splitting devices. *J. Am. Chem. Soc.* **2015,** *137* (13), 4347-4357.

(76) Dai, X.; Du, K.; Li, Z.; Sun, H.; Yang, Y.; Zhang, W.; Zhang, X., Enhanced hydrogen evolution reaction on few–layer $MoS_2$ nanosheets–coated functionalized carbon nanotubes. *Int. J. Hydrogen Energy* **2015,** *40* (29), 8877-8888.

(77) Li, Y.; Wang, H.; Xie, L.; Liang, Y.; Hong, G.; Dai, H., $MoS_2$ nanoparticles grown on graphene: an advanced catalyst for the hydrogen evolution reaction. *J. Am. Chem. Soc.* **2011,** *133* (19), 7296-7299.

(78) Niyitanga, T.; Evans, P. E.; Ekanayake, T.; Dowben, P. A.; Jeong, H. K., Carbon nanotubes-molybdenum disulfide composite for enhanced hydrogen evolution reaction. *J. Electroanal. Chem.* **2019,** *845*, 39-47.

(79) Wang, Q. H.; Kalantar-Zadeh, K.; Kis, A.; Coleman, J. N.; Strano, M. S., Electronics and optoelectronics of two-dimensional transition metal dichalcogenides. *Nat. Nanotechnol.* **2012,** *7* (11), 699-712.

(80) Andrieux, C. P.; Costentin, C.; Di Giovanni, C.; Savéant, J.-M.; Tard, C., Conductive mesoporous catalytic films. Current distortion and performance degradation by dual-phase ohmic drop effects. Analysis and Remedies. *J. Phys. Chem. C* **2016,** *120* (38), 21263-21271.

(81) Costentin, C.; Di Giovanni, C.; Giraud, M.; Savéant, J.-M.; Tard, C., Nanodiffusion in electrocatalytic films. *Nat. Mater.* **2017,** *16* (10), 1016-1021.

(82) Lyons, M. E. G.; McCormack, D. E.; Smyth, O.; Bartlett, P. N., Transport and kinetics in multicomponent chemically modified electrodes. *Faraday Discuss. Chem. Soc.* **1989,** *88* (0), 139-149.

(83) Eftekhari, A., Electrocatalysts for hydrogen evolution reaction. *Int. J. Hydrogen Energy* **2017,** *42* (16), 11053-11077.

(84) Wu, L.; Longo, A.; Dzade, N. Y.; Sharma, A.; Hendrix, M. M. R. M.; Bol, A. A.; de Leeuw, N. H.; Hensen, E. J. M.; Hofmann, J. P., The origin of high activity of amorphous $MoS^2$ in the hydrogen evolution reaction. *ChemSusChem* **2019,** *12* (19), 4383-4389.

(85) Fletcher, S., Tafel slopes from first principles. *J. Solid State Electrochem.* **2009,** *13* (4), 537-549.

(86) Song, F.; Bai, L.; Moysiadou, A.; Lee, S.; Hu, C.; Liardet, L.; Hu, X., Transition metal oxides as electrocatalysts for the oxygen evolution reaction in alkaline solutions: an application-inspired renaissance. *J. Am. Chem. Soc.* **2018,** *140* (25), 7748-7759.

(87) Shinagawa, T.; Garcia-Esparza, A. T.; Takanabe, K., Insight on Tafel slopes from a microkinetic analysis of aqueous electrocatalysis for energy conversion. *Sci. Rep.* **2015,** *5*, 13801-13801.

(88) Kodintsev, I. M.; Trasatti, S., Electrocatalysis of $H_2$ evolution on $RuO_2$ + $IrO_2$ mixed oxide electrodes. *Electrochim. Acta* **1994,** *39* (11), 1803-1808.

(89) Bockris, J. O. M.; Ammar, I. A.; Huq, A. K. M. S., The Mechanism of the hydrogen evolution reaction on platinum, silver and tungsten surfaces in acid solutions. *J. Phys. Chem.* **1957,** *61* (7), 879-886.

(90) Morozan, A.; Goellner, V.; Zitolo, A.; Fonda, E.; Donnadieu, B.; Jones, D.; Jaouen, F., Synergy between molybdenum nitride and gold leading to platinum-like activity for hydrogen evolution. *Phys. Chem. Chem. Phys.* **2015,** *17* (6), 4047-4053.

(91) Tran, P. D.; Nguyen, M.; Pramana, S. S.; Bhattacharjee, A.; Chiam, S. Y.; Fize, J.; Field, M. J.; Artero, V.; Wong, L. H.; Loo, J.; Barber, J., Copper molybdenum sulfide: a new efficient electrocatalyst for hydrogen production from water. *Energy Environ. Sci.* **2012,** *5* (10), 8912-8916.

(92) Antolini, E., Carbon supports for low-temperature fuel cell catalysts. *Appl. Catal. B: Environ.* **2009,** *88* (1), 1-24.

(93) Hoogers, G., *Fuell Cell Technology Handbook*. CRC Press UC, Boca Raton: 2003.

(94) Petrone, R.; Hissel, D.; Péra, M. C.; Chamagne, D.; Gouriveau, R., Accelerated stress test procedures for PEM fuel cells under actual load constraints: State-of-art and proposals. *Int. J. Hydrogen Energy* **2015,** *40* (36), 12489-12505.

(95) Zhang, S.; Yuan, X.; Wang, H.; Mérida, W.; Zhu, H.; Shen, J.; Wu, S.; Zhang, J., A review of accelerated stress tests of MEA durability in PEM fuel cells. *Int. J. Hydrogen Energy* **2009,** *34* (1), 388-404.

(96) Schonvogel, D.; Rastedt, M.; Wagner, P.; Wark, M.; Dyck, A., Impact of accelerated stress tests on high temperature PEMFC degradation. *Fuel Cells* **2016,** *16* (4), 480-489.

(97) Aßmann, P.; Gago, A. S.; Gazdzicki, P.; Friedrich, K. A.; Wark, M., Toward developing accelerated stress tests for proton exchange membrane electrolyzers. *Curr. Opin. Electrochem.* **2020,** *21*, 225-233.

(98) NOVEL Project: Novel materials and system designs for low cost, efficient and durable PEM electrolysers.

(99) Moreno-Hernandez, I. A.; MacFarland, C. A.; Read, C. G.; Papadantonakis, K. M.; Brunschwig, B. S.; Lewis, N. S., Crystalline nickel manganese antimonate as a stable water-oxidation catalyst in aqueous 1.0 M $H_2SO_4$. *Energy Environ. Sci.* **2017,** *10* (10), 2103-2108.

(100)Zhou, L.; Shinde, A.; Montoya, J. H.; Singh, A.; Gul, S.; Yano, J.; Ye, Y.; Crumlin, E. J.; Richter, M. H.; Cooper, J. K.; Stein, H. S.; Haber, J. A.; Persson, K. A.; Gregoire, J. M., Rutile alloys in the Mn–Sb–O system stabilize $Mn^{3+}$ to enable oxygen evolution in strong acid. *ACS Catalysis* **2018,** *8* (12), 10938-10948.

**For Table of Contents only**